Dynamic capillary phenomena using Incompressible SPH

Prapanch Nair *, Thorsten Pöschel

Institute for Multiscale Simulation, Friedrich-Alexander Universität Erlangen-Nürnberg, 91052 Erlangen, Germany

HIGHLIGHTS

- Surface tension and wetting model introduced in an Incompressible SPH with free surface.
- Instability in a splash crown captured without imposed perturbations.
- Critical velocity for dynamic liquid bridge rupture between colliding wet particles obtained through simulations.

ABSTRACT

Grid based fluid simulation methods are not able to solve complex non-linear dynamics like the rupture of a dynamic liquid bridge between freely colliding solids–an exemplary scenario of capillary forces competing with inertial forces in engineering applications–using a monolithic formulation for the solid and liquid phases present. We introduce a new Incompressible Smoothed Particle Hydrodynamics method for simulating three dimensional fluid-solid interaction flows with capillary (wetting and surface tension) effects at free surfaces. This meshless approach presents significant advantages over grid based approaches in terms of being monolithic and in handling interaction with free solids. The method is validated for accuracy and stability in dynamic scenarios involving surface tension and wetting. We then present three dimensional simulations of crown forming instability following the splash of a liquid drop, and the rupture of a liquid bridge between two colliding solid spheres, to show the method's advantages in the study of dynamic micromechanical phenomena involving capillary flows.

© 2017 Elsevier Ltd. All rights reserved.

1. Introduction

Appreciation of non-linear micro mechanical phenomena is crucial to advance the efficiency of many production processes that are aided by the presence of a momentary liquid phase. Processes such as wet fluidized beds (Mikami et al., 1998), powder agglomeration (Hussain et al., 2013), pelletizing (Tsunazawa et al., 2016) and spray painting (Ye et al., 2005) in industrial scales are essentially multiscale phenomena where the macroscopic behaviour is predicted by simulations using simple analytical models for the smaller scale mechanics. Improving the understanding of micromechanics using well resolved simulations is crucial to improve the models employed in macroscopic simulations. Dynamic capillary scenarios in small scales are difficult to study experimentally and traditional fluid simulation methods have their limitations and therefore there is an increasing interest in exploring meshless approaches.

Traditional multiphase flow simulation methods employing the Volume of fluid (VOF) method (Hirt and Nichols, 1981), Constraint interpolation method (CIP) (Yabe et al., 2001), Level set or Coupled Level set VOF methods (Tomar et al., 2005) are increasingly used to simulate such phenomena. However, they have their limitations in handling high density ratio or free surfaces (Popinet, 2009), moving three-phase contact line consistent with a no-slip wall (Renardy et al., 2001; DussanV, 1976) and interacting solids with all six degrees of freedom. While higher order consistency is easy to achieve in Eulerian methods, multi component simulations require coupling of different numerical approaches (for example, the Immersed Boundary Method (Peskin, 2002)) limiting the ease of set up of these simulations.

Meshless Lagrangian simulation methods, for example the Smoothed Particle Hydrodynamics (SPH) and its derivatives, have the advantage of handling complex shaped free surfaces (Monaghan, 1994)—a better approximation to a typical liquid-air system than a finite density ratio and explicit interactions with solids (Nair and Tomar, 2014; Nair and Tomar, 2017). While free surfaces are implicitly handled by traditional SPH methods with a weak compressibility model, they require non-trivial treatment in case of the more accurate Incompressible SPH (ISPH) methods (Lee et al., 2008), which solves for a pressure field for strict

* Corresponding author.
    E-mail address: prapanch.nair@fau.de (P. Nair).

incompressibility. An accurate semi-analytic free surface model for ISPH was implemented recently (Nair and Tomar, 2014), expanding the scope of this more accurate version of SPH. Particularly, this approach allows finite pressure gradients close to the free surface making it possible to couple different interface tension models to the free surface.

Surface tension was initially implemented in SPH using a Continuum Surface Force (CSF) model (Brackbill et al., 1992; Morris, 2000), following Eulerian two phase flow simulation methods (Brackbill et al., 1992). Since then CSF based surface tension models in SPH have improved considerably in accuracy and stability (Adami et al., 2010; Colagrossi and Landrini, 2003). In CSF, the surface tension force is modeled as a volumetric force proportional to the interface curvature, which in turn is obtained by computation of divergence of normalized gradient of the Heaviside step function (Morris, 2000) or by geometrically reconstructing the interface (Zhang, 2010). While the former is limited in its application to interfaces with fluid on both sides (with exceptions which use kernel corrections (Hirschler et al., 2017)), the latter requires expensive computations to identify particles at the interface (Zhang, 2010). Inspired by the molecular origin of surface tension phenomena, a model based on pair-wise forces was introduced by Nugent and Posch (2000) for a van der Waals liquid drop. This approach was further improved in Tartakovsky and Meakin (2005) and applied to a number of free surface problems. Such approaches are also used in computer graphics research for emulating optically plausible behaviour with considerably less computational cost (Akinci et al., 2013). In a recent work (Tartakovsky and Panchenko, 2016), the relations between macroscopic parameters like surface tension coefficient and apparent contact angle to the strength and nature of the pairwise particle forces was elucidated. In this work, a number of validation cases were presented by the authors establishing the method as an accurate surface tension model of engineering importance. The application of the pairwise force model has been mostly limited to the weakly compressible version of SPH. Some works also have employed the pairwise model to ISPH flows involving free surfaces (Säckel and Nieken, 2016; Aly et al., 2013). However, the free surface models employed in these works are based on heuristic identification of particles at free surface. Setting a fixed constant pressure at a layer of particles at the free surface restricts tangential pressure gradients that result from capillary forces, near the free surface. Also much of the complexities of this approach such as the effect of the cut off radius of the pairwise forces and that of background pressure due to the pairwise forces on the accuracy of the ISPH method have not been addressed and validated.

In the present paper, we present a novel ISPH method that couples an accurate free surface model to a pairwise force capillary model to simulate dynamic capillary effects. The relation between inter particle force strengths and the macroscopic parameters like surface tension and contact angle are given for free surfaces. Different aspects of the method such as dynamics due to surface tension, contact angle and capillary force balance, are separately validated.

We then apply the method to the simulation of two three dimensional problems exemplary of dynamic capillary effects. First, we observe the onset of instability and the breaking of symmetry following splash of a drop on a liquid film. Second, we obtain the critical velocity for agglomeration of two colliding wet solids by observing the rupture of the liquid bridges as the solids depart and compare it with theoretical results.

2. ISPH formulation

The governing equation and SPH discretization used for incompressible fluids with free surface is presented here. The philosophy

and basic formulation of the SPH method can be found in a number of works, for example Violeau (2012), and here we present only the SPH approximations that are relevant to the presented method.

2.1. Governing equations

Momentum conservation equations for a Newtonian fluid are solved using the SPH method in an updated-Lagrangian frame of reference. By updated we mean that the reference configuration for application of constitutive relation of the material is updated with time, as opposed to a purely Lagrangian method where the reference configuration is a relaxed initial state. The Navier-Stokes equations governing the momentum conservation of incompressible isothermal flow are given by,

$$\frac{d\mathbf{u}}{dt} = \frac{1}{\rho}(-\nabla p + \nabla \cdot (2\mu \mathbf{D})) + \mathbf{f}^B, \qquad (1)$$

where $\mathbf{u}$ is the velocity, p is the pressure, ρ is the density, μ is the coefficient of viscosity of the fluid, $\mathbf{D} = (\nabla \mathbf{u} + \nabla \mathbf{u}^T)/2$ is the deformation rate tensor, $\mathbf{f}^B$ is the body force per unit mass on the fluid element and t is the time. The Navier-Stokes equation has been written in the Lagrangian formulation and d/dt denotes the material derivative. The mass conservation equation for incompressible flows is given by,

$$\nabla \cdot \mathbf{u} = 0. \qquad (2)$$

The governing equations are discretized on a particle domain in SPH. As a model for surface tension, a molecular dynamics inspired pairwise force model (Tartakovsky and Panchenko, 2016) is superimposed on the particle system following the observation that molecular forces are superposable on forces derived from momentum conservation equations on the same particle system (Nugent and Posch, 2000).

2.2. SPH formulation

The SPH discretization of the governing Eq. (1) together with a pairwise force model (Tartakovsky and Panchenko, 2016) is as follows:

$$\left.\frac{d\mathbf{u}}{dt}\right|_a = -\sum_b m_b \frac{p_a + p_b}{\rho_a \rho_b} \nabla_a W_{ab}$$
$$+ \sum_b m_b \left(\frac{\mu_a + \mu_b}{(\rho_a \rho_b)} \frac{\mathbf{r}_{ab} \cdot \nabla_a W_{ab}}{r_{ab}^2 + \epsilon^2}\right) \mathbf{u}_{ab} + \mathbf{f}_a^{\text{int}} + \mathbf{f}_a^B, \qquad (3)$$

where m is the mass, ρ is the density, p is the pressure, at a particle identified by the subscript a or its neighbor b. Here $\mathbf{r}_{ab}$ is the displacement vector between particles a and b and r_{ab}, its magnitude. The function W is the symmetric and positive definite smoothing function, also known as the kernel for the SPH discretization defined for a particle pair as $W_{ab} = W(r_{ab}, h)$, where h is the smoothing length of the kernel. The kernel has a compact support and its domain is cut off by a factor q_{cutoff} times the smoothing length h in space. The pairwise forces $\mathbf{f}_{ab}^{\text{int}}$, applied to simulate interfacial force is explained in Section 2.4 and $\mathbf{f}_a^B$ denotes the body force per unit mass acting on particle a and represents the gravitational acceleration in the present work. We use a viscous force approximation (the second term on the right hand side) that is extensively used in SPH literature (Morris et al., 1997). In this term, $\mathbf{u}_{ab}$ is the relative velocity vector between particles a and b, ϵ is a small positive number (usually chosen as $(0.01h)^2$) to avoid division by zero for a rare incident of particles overlapping each other and μ is the coefficient of viscosity with its subscript denoting the corresponding SPH particle. The pressure gradient approximation (the first

term on the right hand side) is chosen to be one applicable to multiphase flow problems (Colagrossi et al., 2013; Szewc et al., 2012).

Near solid walls, the gradient and divergence approximations require a filled kernel neighborhood. This is achieved by distributing static particles along solid walls with the same particle spacing as in the initial spacing of fluid particles. These wall particles can be modeled as belonging to rigid bodies to simulate free solids interacting with the liquid. Such an approach conserves linear and angular momentum and can be seen by a force balance across the solid-liquid interface as explained in Nair and Tomar (2014).

At free surfaces, standard weakly compressible SPH is known to naturally satisfy a zero pressure Dirichlet boundary condition corresponding to a moving interface (Monaghan, 1994) if a conservative pressure gradient approximation is used. However, explicit application of Dirichlet boundary condition is necessary if a pressure solver is invoked to compute the pressure field. It is important for the Dirichlet boundary condition to be applied in a consistent and accurate manner to preserve the accuracy of ISPH.

2.3. ISPH and the free surface formulation

Following grid based methods for incompressible flows, where a divergence free constraint is imposed on velocity field, ISPH solves for the pressure Poisson equation

$$\nabla \cdot \left(\frac{\nabla p}{\rho} \right) = \frac{\nabla \cdot \mathbf{u}}{\Delta t}, \tag{4}$$

on the particle domain. The SPH discretization of this equation (Lee et al., 2008) is:

$$\sum_b \frac{m_b}{\rho_b} \frac{4}{\rho_a + \rho_b} (P_a - P_b) \frac{\mathbf{r}_{ab} \cdot \nabla_a W_{ab}}{r_{ab}^2 + \epsilon^2} = -\frac{1}{\rho_a} \sum_b m_b \mathbf{u}_{ab} \cdot \nabla_a W_{ab}. \tag{5}$$

When a linear system is solved on the particle domain to obtain pressure, application of Dirichlet boundary condition for pressure is necessary. A semi-analytic model was introduced in a previous work (Nair and Tomar, 2014) to implement free surface Dirichlet boundary condition with greater accuracy and robustness over previous approaches involving identification of free surface particles (Lee et al., 2008; Violeau and Rogers, 2016). This model is implemented by modifying the linear system for solving the pressure Poisson equation in the SPH particle domain as:

$$\nabla \cdot \left(\frac{\nabla p}{\rho} \right) \Big|_a = (p_a - p_o)\kappa - \sum_{b_i} \frac{m_b}{\rho_b} \frac{4}{\rho_a + \rho_b} p_b \frac{\mathbf{r}_{ab} \cdot \nabla_a W_{ab}}{r_{ab}^2 + \epsilon^2}$$
$$+ \sum_{b_i} \frac{m_b}{\rho_b} \frac{4}{\rho_a + \rho_b} p_o \frac{\mathbf{r}_{ab} \cdot \nabla_a W_{ab}}{r_{ab}^2 + \epsilon^2} \tag{6}$$

where p_0 represents the ambient pressure and κ, given by

$$\kappa = \sum_b \frac{m_b}{\rho_b} \frac{4}{\rho_a + \rho_b} \frac{\mathbf{r}_{ab} \cdot \nabla_a W_{ab}}{r_{ab}^2 + \epsilon^2}, \tag{7}$$

represents a kernel completion factor. Here b_i represents the particles in the actual neighborhood of a and b represents an exemplary full kernel neighborhood of a (as if a were in the interior of the fluid domain). Then the deficiency in the Laplacian operator term that arises due to the truncation of the kernel for a particle near the free surface is computed by subtracting the computed Laplacian operator from the Laplacian operator in the bulk (κ). A constant Dirichlet pressure is supplied with this deficiency term, thus constituting the Dirichlet boundary condition. The details and derivation of the above equations can be found in Nair and Tomar (2014). The kernel completion factor can be computed analytically for a given kernel function and discretization parameters. However, in the present work, similar to Nair and Tomar (2014), we compute this term numerically in order to maintain the same order of accuracy as

the discretization scheme. The term needs to be computed only once based on the discretization parameters and smoothing function for the entire simulation.

For incompressible free surface simulations, the pressure gradient and not the value of pressure appears in the governing equations and hence a zero pressure Dirichlet boundary condition is sufficient. For zero Dirichlet Pressure the above free surface model simply modifies the terms in the leading diagonal of the linear system for pressure for those particles that face a kernel deficiency due to proximity to free surface. For non-zero Dirichlet pressure values, the model introduces additional terms to the right hand side of the linear system.

The time integration of the field variables are performed by a velocity Verlet integration algorithm (Allen and Tildesley, 1989) given by:

$$\mathbf{r}_a(t + \Delta t) = \mathbf{r}_a(t) + \Delta t \mathbf{u}_a(t) + \frac{\Delta t^2}{2} \mathbf{f}_a^{\text{tot}}(t) \tag{8}$$

$$\mathbf{u}_a(t + \Delta t) = \mathbf{u}_a(t) + \frac{\Delta t}{2} \left(\mathbf{f}_a^{\text{tot}}(t) + \mathbf{f}_a^{\text{tot}}(t + \Delta t) \right). \tag{9}$$

Here, $\mathbf{f}_a^{\text{tot}}$ is the total acceleration of a particle a contributed by both continuum (viscous, pressure, body forces) and inter-particle forces. The integration time step Δt is set to satisfy the following constraint for numerical stability (Tartakovsky and Panchenko, 2016):

$$\Delta t \leqslant \min_a \left(0.25 \frac{h}{3|\mathbf{u}_a|}, 0.25 \sqrt{\frac{m_a h}{3|\mathbf{f}_a^{\text{int}}|}}, 0.25 \frac{\rho h^2}{9\mu} \right). \tag{10}$$

2.4. Pairwise-force model for free surface ISPH

The pairwise force required to model capillary effects needs to be repulsive in the short range and attractive in the long range and may be much less stiffer than the potentials used in molecular dynamics simulations (Rowlinson and Widom, 2013). The inter-particle acceleration term that appears in Eq. (3) is given by:

$$\mathbf{f}_a^{\text{int}} = \sum_b \frac{F_{\alpha\beta}^{\text{int}}(r_{ab})}{m_a} \frac{\mathbf{r}_{ab}}{r_{ab}}, \tag{11}$$

where α and β represent the phases of the particles a and b, respectively, separated by a vector $\mathbf{r}_{ab}$ in space. The pairwise force magnitude as a function of displacement between particles is given as Tartakovsky and Meakin (2005):

$$F_{\alpha\beta}^{\text{int}}(r_{ab}) = \begin{cases} -s_{\alpha\beta} \cos\left(\frac{3\pi}{4} q_{ab}\right) & q_{ab} = \frac{r_{ab}}{h'} \leqslant q_{\text{cutoff}} \\ 0 & q_{ab} = \frac{r_{ab}}{h'} > q_{\text{cutoff}}, \end{cases} \tag{12}$$

where q_{cutoff} is the ratio of cut off length of the kernel to the parameter h', which can be defined in relation to the kernel smoothing length h. Here, we have chosen an SPH kernel with cut-off length to be twice the smoothing length h and the cut-off length of the pairwise force is also set to be equal to that of the SPH kernel. Therefore $h' = h$ and $q_{\text{cutoff}} = 2.0$. Also, $s_{\alpha\beta}$ is the interaction strength between particles of phases α and β respectively. The pairwise force function used throughout this paper is shown in Fig. 1. Symmetry in the strength ensures conservation of linear momentum between particles, ensuring conservation of linear momentum in the SPH discretization. The pairwise force based SPH model is becoming increasingly popular (Tartakovsky and Meakin, 2005, 2006; Liu and Liu, 2010) in literature owing to its ease of application and robustness. In a recent work (Tartakovsky and Panchenko, 2016) a detailed explanation on how the macroscopic parameters such as surface tension, contact angle and the pressure resulting from pairwise forces, called the 'virial pressure' can be related to the strength of the pairwise forces is provided. This approach was also applied to
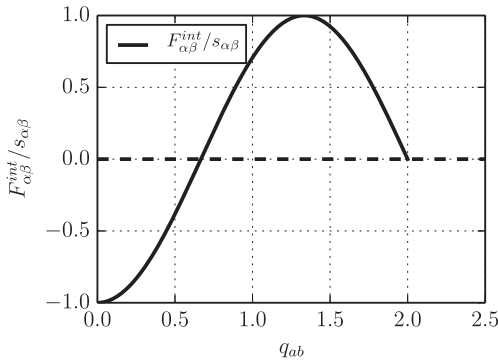
Fig. 1. Pairwise force function with compact support.

free surface flows in earlier works (Nugent and Posch, 2000; Tartakovsky and Meakin, 2005). However the application has been mostly limited to weakly compressible SPH solvers. With the employment of empirical free surface corrections for pressure (Bøckmann et al., 2012), the pairwise force capillary model is implemented in ISPH and applied to simulate engineering processes such as spray drying, in a recent work (Säckel and Nieken, 2016). In the present work the pairwise force model is applied to the ISPH algorithm with the free surface treatment presented in the previous section.

The stress at a given point in a particle system with given pairwise forces can be computed according to the Hardy's formula (Rowlinson and Widom, 2013). This formula is given as a sum of stress due to inter-particle forces and the convection of particles. In the present work, since a hydrodynamic governing equation is used to model the fluid, only the stress due to inter-particle forces becomes relevant, and is given by:

$$\mathbf{T}_{\text{int}}(x) = \frac{1}{2}\sum_{a=1}^{N}\sum_{b=1}^{N}\mathbf{f}_{ab}\otimes(\mathbf{r}_a - \mathbf{r}_b)\int_0^1\tilde{\psi}_\eta(\mathbf{x} - s\mathbf{r}_a - (1-s)\mathbf{r}_b)ds, \quad (13)$$

where $\mathbf{f}_{ab}$ is the force between two particles which in this case is the pairwise force between particle a and b given by Eq. (12); the function $\tilde{\psi}$ is a weighting function with a compact support η which should be greater than the SPH smoothing length h. Following (Tartakovsky and Panchenko, 2016), ψ_η is chosen to be the product of constant valued functions with compact support η, in each spatial dimension. Thus,

$$\tilde{\psi}_\eta(\mathbf{x}) = \prod_l^v \psi_\eta(x_l), \quad (14)$$

where v is the spatial dimension, and

$$\psi_\eta(x_l) = \frac{1}{\eta}\psi\left(\frac{x}{\eta}\right), \quad \psi(x_l) = \begin{cases} 1 & \text{if } x_l \in (-1/2, 1/2), \\ 0 & \text{otherwise.} \end{cases} \quad (15)$$

It is convenient to set the cut off radius for both the pairwise forces and the SPH kernel to the same value. In this work we have uniformly set the cut off length to be two times the smoothing length h, $q_{\text{cutoff}} = 2$. The surface tension at the interface between two phases α and β can be obtained by integration of the tangential stress components along a coordinate, say z, perpendicular to the interface as

$$\sigma_{\alpha\beta} = \int_{-\infty}^{+\infty}[T_\tau(z) - T_n(z)]dz. \quad (16)$$

Here, $T_\tau(z)$ and $T_n(z)$ are the tangential and normal components of the stress when the z coordinate is perpendicular to the interface. Invoking Eq. (13) we write

$$\sigma_{\alpha\beta} = \mathcal{T}_{\alpha\alpha} + \mathcal{T}_{\beta\beta} - 2\mathcal{T}_{\alpha\beta}, \quad (17)$$

where the integrals of tangential stress components due to interaction force between particles of phases $\alpha - \alpha$, $\beta - \beta$ and $\alpha - \beta$ are represented by $\mathcal{T}_{\alpha\alpha}, \mathcal{T}_{\beta\beta}$ and $\mathcal{T}_{\alpha\beta}$ respectively. For a given smoothing kernel $\phi(r)$, these components are derived in the appendix of Tartakovsky and Panchenko (2016). For the free surface problems that are of interest to the present work, where only one liquid phase ($\alpha = l$) is present, the surface tension can be related to the pairwise force as follows for 2D and 3D cases:

$$\mathcal{T}_{ll}^{(2D)} = -\frac{1}{6}\pi\left(\frac{\rho_l}{m_l}\right)^2\int_0^\infty z^3 F_{ll}^{\text{int}}(z)dz, \quad (18)$$

$$\mathcal{T}_{ll}^{(3D)} = -\frac{1}{16}\pi\left(\frac{\rho_l}{m_l}\right)^2\int_0^\infty z^4 F_{ll}^{\text{int}}(z)dz. \quad (19)$$

where z is the coordinate in the direction perpendicular to the interface, and m_l and ρ_l are the mass and density of particles representing the phase, l.

One important assumption being made in the above derivations is that the stresses are integrated across a plane interface, which in effect amounts to having a radius of curvature much larger than the smoothing length. For the specific piece-wise force function we use in our simulations given by Eq. (12), the relation between strength of the force between two liquid particles s_{11} and the surface tension coefficient σ can be derived by substituting the stresses given by Eqs. (18) and (19) in Eq. (17) for a single phase l, since only one liquid phase is present in our free surface formulation:

$$\sigma = \lambda s_{ll}(q_{\text{cutoff}}h_r)^4, \quad \text{for 2D and} \quad (20)$$

$$\sigma = \lambda s_{ll}\frac{(q_{\text{cutoff}}h_r)^5}{\Delta x} \quad \text{for 3D}, \quad (21)$$

respectively. Here, $h_r = h/\Delta x$, is the ratio of the smoothing length of the kernel to the initial particle spacing Δx (here we use a square lattice arrangement of particles) which we refer to as the 'smoothing resolution.' Note that these expressions correspond to the specific choice of pairwise force function and compact support given in Section 2.4. The constant due to integration of the pairwise force function, λ takes the value 0.0476 in 2 dimensions and 0.0135π in 3 dimensions, respectively, for the interaction function given by Eq. (12). Note the occurrence of the absolute value of initial particle spacing in the three dimensional version of this relation.

The pairwise force model also introduces an artificial 'virial pressure.' Even at a plane interface, the particles near the interface are attracted to the particles in the bulk and this introduces an additional virial pressure in addition to the Laplace pressure that results when the interface has a finite curvature. This pressure can be computed for a given particle configuration and pairwise force function from the following equation:

$$p_l^v = -\frac{1}{2}\pi\left(\frac{\rho_l}{m_l}\right)\int_0^\infty z^2 F_{ll}^{\text{int}}(z)dz \quad (22)$$

$$p_l^v = -\frac{2}{3}\pi\left(\frac{\rho_l}{m_l}\right)\int_0^\infty z^3 F_{ll}^{\text{int}}(z)dz \quad (23)$$

for two and three dimensions, respectively, following the derivation given in Tartakovsky and Panchenko (2016). For the incompressible flows that are of interest to the present work, this pressure is additive to the hydrodynamic pressure computed to satisfy incompressibility. Hence, this pressure can be computed and subtracted from the pressure obtained from solving the linear system given by Eq. (5). The contact angle made by the liquid with a solid substrate can then be controlled by appropriate ratio of pairwise force strength between particles of different phases. In the present scenario liquid and solid phase alone are considered. The contact angle can be computed from a surface energy balance for surface energy

between free surface and solid liquid interface. The contact angle is given by Tartakovsky and Panchenko (2016):

$$\cos\theta_0 = \frac{-s_{ll} + 2s_{ls}}{s_{ll}}, \tag{24}$$

where θ_0 is the contact angle made by the liquid free surface with the solid substrate, s_{ll} and s_{ls} ($\alpha = l$ and $\beta = s$) are the strengths of the pairwise force for liquid-liquid particle pairs and liquid–solid particle pairs respectively. The above equation is a simplification of the contact angle expression given in Eq. 60 of Tartakovsky and Panchenko (2016) repeated here:

$$\cos\theta_0 = \frac{s_{\beta\beta} - s_{\alpha\alpha} - 2s_{\beta s} + 2s_{\alpha s}}{s_{\alpha\alpha} + s_{\beta\beta} - 2s_{\alpha\beta}}, \tag{25}$$

where α and β are the two fluid phases and s is the solid phase. In our simulations we use only the terms involving α and s and replace the subscript α with l to obtain Eq. (24).

Smoothed Particle Hydrodynamics approximation of the momentum equation is similar in form to a particle system with inter-particle forces explicitly defined between particles. Using the concept of composite particles, (Violeau, 2012) shows that a pressure force term can be derived similar in form to SPH pressure gradient, which also implies that a different set of inter-particle forces can be superimposed on the SPH particle system consistently. For ISPH this may be even more relevant since the pressure field is smoother in general than weakly compressible SPH methods (Lee et al., 2008).

3. Validation and results

The above introduced capillary model based on pairwise forces applied at free surfaces coupled by the dynamics simulated by ISPH is a novel method and therefore requires careful validation before application to realistic scenarios. We first present validations of the above described ISPH free surface capillary model using 2D and 3D simulations. We solve dynamic test cases where the absolute value of pressure modified by the presence of pairwise forces (virial pressure as in Eq. (23)) is unimportant, as the dynamics would be determined by the pressure gradient on a constant density domain. Oscillating drop test cases are presented in 2 and 3 dimensions to validate the macroscopic surface tension coefficient against the strength of the pairwise potential. Contact angles are measured at steady state and during transient states of relaxation of a sessile droplet on a plane surface. Capillary rise of liquid through a capillary tube is also simulated to check for the model's capability to handle surface tension and contact angles in the same domain. We then use the algorithm to simulate the impact of a drop of liquid on a liquid film in order to observe the onset of instability and the breakage of axial symmetry leading to the formation of a splash crown in three dimensions. Finally, together with a solid interaction algorithm, we use the method to simulate rupture/sustenance of liquid bridges following collision of solid spheres of industrially relevant dimensions with wet spots, in order to demonstrate the promise of the algorithm in handling arbitrary geometries. We use the Wendland kernel (Wendland, 1995) for all the test cases presented here, owing to its superior numerical stability properties (Dehnen and Aly, 2012; Szewc et al., 2012). In Sections 3.1 and 3.2, we have not provided specific units in our plots, since arbitrary units could be used without changing the results.

3.1. Oscillation of a liquid drop

The surface tension coefficient for a given particle configuration can be verified by computing the frequency of oscillation of a drop of fluid about its circular (in 2D) or spherical (in 3D) minimal area

reference geometry. The time period of oscillation for an inviscid infinite cylindrical jet is given by Nugent and Posch (2000) based on the general results of Rayleigh Rayleigh (1879) as:

$$T = 2\pi\sqrt{\frac{R^3\rho}{6\sigma}}. \tag{26}$$

For three dimensions, the frequency of shape oscillation (second mode) of a drop is given by:

$$T = \pi\sqrt{\frac{R^3\rho}{2\sigma}}, \tag{27}$$

where T is the time period of oscillation, ρ is the density of the liquid, R is the radius of the drop and σ is the surface tension coefficient.

Surface tension can thus be measured from these equations by measuring the time period of oscillation of a drop, initially perturbed to an ellipse (or ellipsoid) of equal volume. The time response of the radius of the infinite 2D cylinder and sphere are shown in Fig. 2. The simulation experiment is repeated with liquid drops of different densities and pairwise force strengths for 2D and these results are plotted in Fig. 3a, and in 3D (Fig. 3b) this linear relation is shown to hold good across orders of magnitude of pairwise force strengths. The results show that the relation between potential strength and surface tension is indeed linear, as seen in Eq. (21). In these validation cases the smoothing length h is chosen such that $h/\Delta x = 3.75$, where Δx is the initial particle spacing. This 'smoothing resolution,' $h_r = h/\Delta x$, is indeed much higher than what is recommended in SPH literature (Szewc et al., 2012). Even for pairwise force models, previous studies (Tartakovsky and Meakin, 2005) have employed smaller smoothing resolution. However, for simulating dynamic capillary phenomena using the pairwise-force model we show that a higher smoothing resolution and therefore larger number of particles in the support domain is needed. In Fig. 4 we present the response of the oscillating drop in 2D for different spatial resolutions and smoothing resolutions. The initial shape of the drop is chosen to be an ellipse with major axis lenth $A = 2.0$ and minor axis length $B = 1.6$. In Fig. 4a and b, we see that oscillation profiles and the frequency predictions remain observably similar for increasing spatial resolution for 40, 80 and 160 particles along the initial major axis length A, simulated for a fixed smoothing resolution of $h_r = 3.75$.

In Fig. 4c, we maintain the same spatial resolution ($A/\Delta x = 40$) while varying the smoothing resolution, h_r. We see that as h_r goes below 2.75, the oscillations damp within the first oscillation itself and the drop does not reach its expected equilibrium shape. However for higher smoothing resolution, the frequency of the droplet is predicted accurately as show in Fig. 4d by the peaks coinciding with the dashed line, which indicates the frequency of oscillation computed from Eq. (26).

In surface tension dominant problems the time step would be determined by the criteria based on the pairwise force strengths, corresponding to the second term in Eq. (10). Since the pairwise force varies as $1/h_r^4$ as shown in Eq. (20), for smaller h_r, the time step decreases as $h_r^{5/2}$ according to the time step limitation given by condition 10. Therefore, smaller smoothing resolution requires large pairwise force strength for a given surface tension coefficient, and incidentally requires smaller timesteps. This is in contrast to the SPH scheme itself where a smaller smoothing resolution (implying smaller h for given Δx) decreases the time step linearly. Hence large smoothing resolution (> 2.75) is necessary for accuracy and feasibility of the pairwise-force model. The loss in accuracy for low smoothing resolution may be explained by energy considerations.
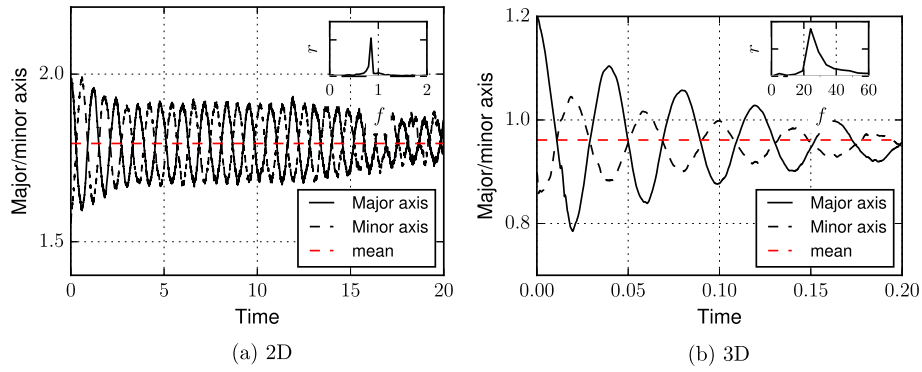
Fig. 2. Time response of radii of an oscillating drop about its reference configuration in 2D and 3D. Insets show the frequency domain of oscillation, showing the frequency of oscillation.
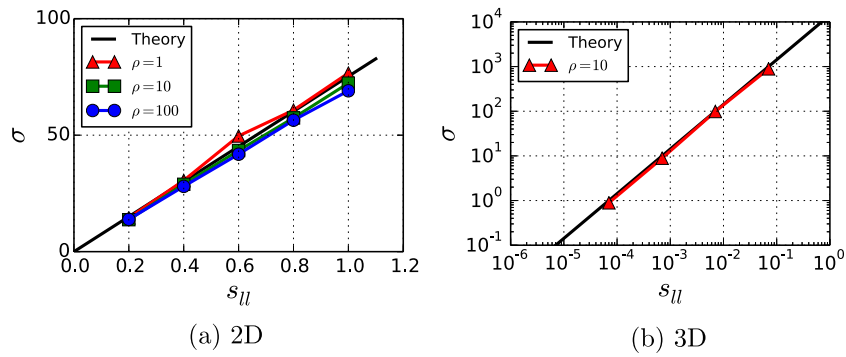

Fig. 3. Linear variation of surface tension coefficient with strength of pairwise potential. The solid black line is obtained from Eq. (18). For the 2D cases, different densities were considered for the oscillating drop, and potential strengths across orders of magnitude were used in the 3D cases.
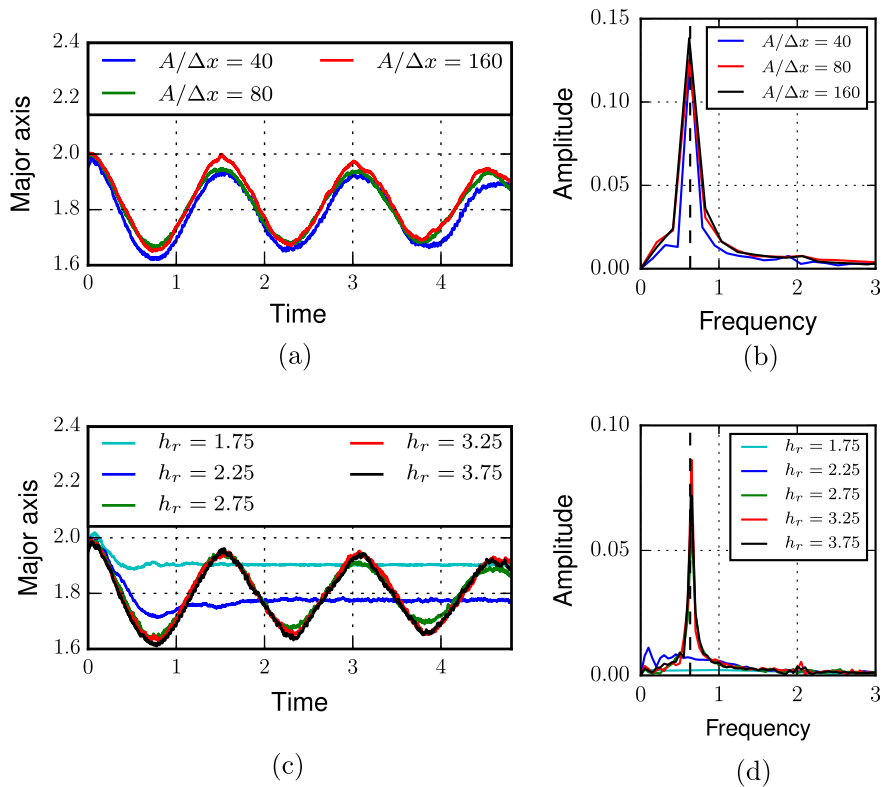

Fig. 4. Resolution study (2D): (a) and (c) Time response of the major axis length of an elliptical drop at different times for different spatial resolutions ($A/\Delta x$) and smoothing resolutions ($h_r = h/\Delta x$), respectively. (b) and (d) Frequency domain of the oscillation of the drop for different spatial resolutions and smoothing resolutions, respectively; vertical dashed line corresponds to the theoretical frequency of oscillation.

For smaller smoothing resolution, the particles tend to 'crystallize' to lower energy configurations, causing the above observed overdamping of the system. To assert this, we present the fluctuation kinetic energy normalized by the kinetic energy in the mean flow, defined as:

$$\widehat{E}' = \frac{\sum_a |\mathbf{u}_a - \sum_b \mathbf{u}_b W_{ab} \frac{m_b}{\rho_b}|^2}{\sum_a |\sum_b \mathbf{u}_b W_{ab} \frac{m_b}{\rho_b}|^2}, \tag{28}$$

where $\mathbf{u}_a$ is the velocity of a particle a, b represents the particles in the neighborhood of a including itself. The term $\sum_b \mathbf{u}_b W_{ab} m_b / \rho_b$ is a measure of the meanflow velocity and was introduced by Monaghan in Monaghan (1989) and is widely used in a popular version of SPH known as XSPH. As seen in Fig. 5, the normalized fluctuation kinetic energy $\widehat{E}'$ remains high for higher smoothing resolution ($h_r = 3.75$) and has a spectrum with no noticeable peaks as seen in the inset in the figure. Also the kinetic energy of fluctuations remains an order of magnitude higher than the total kinetic energy in the mean flow. In the case of smaller smoothing resolution ($h_r = 1.25$), the fluctuation kinetic energy is much lower implying local crystallization of particles, overdamping the dynamics of the drop. The fluctuating and mean velocity components of the particles in the same spatial location and time instance (after a few drop oscillations) are show in Fig. 6. In the case of larger smoothing resolution of $h_r = 3.75$, the mean flow profile looks smooth showing that the fluctuating components do not have an effect on the underlying mean flow as seen in Fig. 6a and b. However, for smaller smoothing resolution $h_r = 1.25$, the mean flow profile has considerable noise (Fig. 6d), and as seen in Fig. 5, the kinetic energy of fluctuations are close to the kinetic energy of the mean flow. The effect of the pairwise forces, however, on the viscosity of the fluid for various smoothing resolutions require deeper understanding and this will be part of a future work. Based on the above observations we proceed with a high smoothing resolution of $h_r > 2.75$ for all the further simulations presented. The ability of the method to simulate surface tension and resulting dynamic response for many practical applications is quite promising if care is taken to include enough particles in the support domain of the pairwise force, based on the results of the presented validations.

3.2. Validation of the contact angle model

The contact angle and incidental wetting behaviour can be controlled in the pairwise force ISPH by varying the relative potential strengths between particles of different phases according to Eq. (24). A droplet (in 2D and 3D) initially in a hemispherical configuration (semicircle in 2D) is placed on a solid substrate and is allowed to relax. In the case of dewetting contact angles ($> 90°$), a gravitational body force was applied on the particle to prevent it from bouncing off. After steady state was reached, a layer of particles lying on the free surface were obtained by a kernel summation criteria and first six particles close to the contact point were chosen and regressed linearly to obtain the apparent contact angle θ_s. Fig. 7a and b show the profile of the drop for different potential strength pairs. The bracketed values show the expected contact angles computed by Eq. (24) in this figure. The resolution and geometry of the drop is similar to the previous validation case for oscillating drops.

In order to demonstrate the evolution of the contact angle with time, we show in Fig. 8, the time variation of the contact angle (measured similar to the steady state contact angles) for an dewetting and a wetting case from the 3D simulations. The plot shows that the angle remains reasonably steady with minor oscillations about its expected value during the relaxation of the drop. This is in contrast to contact angle heuristically applied in case of a traditional mesh based CFD method with a sharp interface model such as the volume of fluids (VOF) method. The pressure field within the sessile drop as it relaxes to the equilibrium is shown in Fig. 9. The initial hemispherical configuration (Fig. 9a) begins to spread out (Fig. 9b) until it reaches a maximum wetted area (Fig. 9c). After several oscillations, the drop reaches an equilibrium profile (Fig. 9d). The axial symmetry breaks and due to the fluctuations in the velocity field as presented in the test case of oscillating drops, the pressure field also breaks its axi-symmetry and fluctuations continue to exist even after the drop reaches an equilibrium profile.

3.3. Capillary rise in 2D

Capillary rise of a liquid through a capillary tube is an intricate and useful phenomenon for which analytical solution is straightforward. We construct a simple 2D domain periodic in the horizontal direction with a capillary tube inserted into it. A contact angle of $30°$ is chosen in these test case, and is performed for different tube diameters. The initial particle spacing is set at $0.03125\ mm$ with a smoothing length 3.5 times the spacing.

The height of capillary liquid column with respect to the liquid level outside the capillary tube for different capillary diameters can be found in Table 1 and the steady state of the simulation for these cases can be seen in Fig. 10. The method predicts the rise of the liquid column reasonably accurately, giving confidence for simulations involving surface tension and wetting and their combined effects.
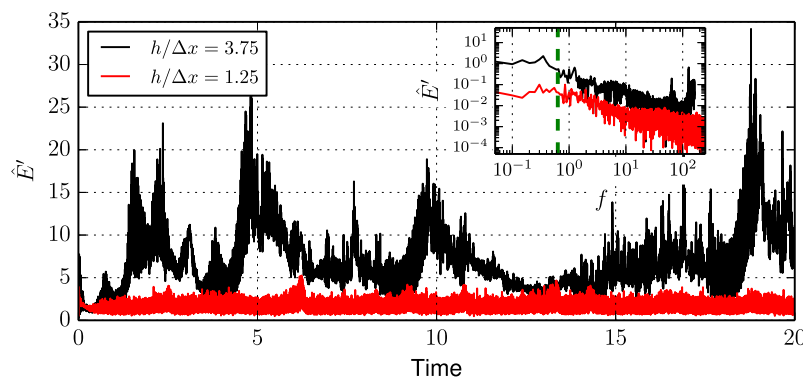

Fig. 5. Variation of kinetic energy of fluctuations (Eq. (28)) of a particle with time, for two different smoothing lengths. Inset shows the presence of high frequency components in the frequency domain of the signals, due to the superimposed inter-particle forces. Vertical green dashed line corresponds to the frequency of oscillation of the drop.
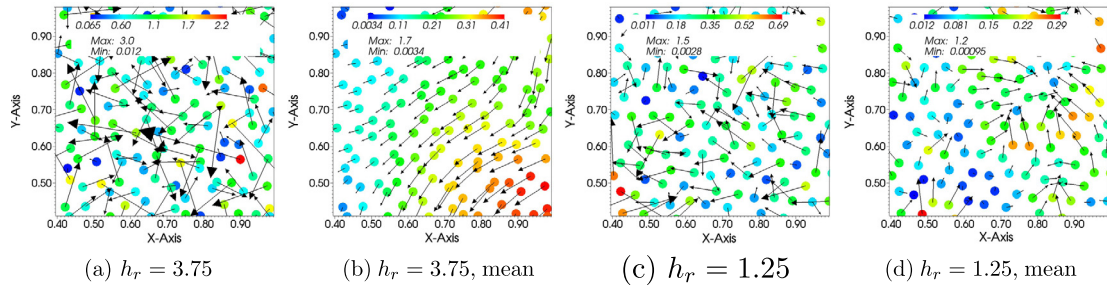
Fig. 6. Particle velocities and mean flow velocities for different smoothing resolutions.
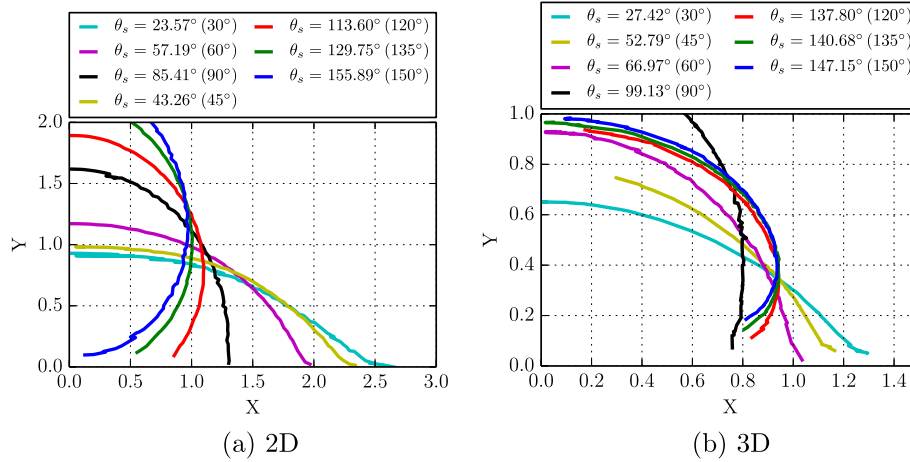

Fig. 7. Contact angles of a sessile drop measured for different potential strength ratios. Values in brackets are the expected angles according to Eq. (24)
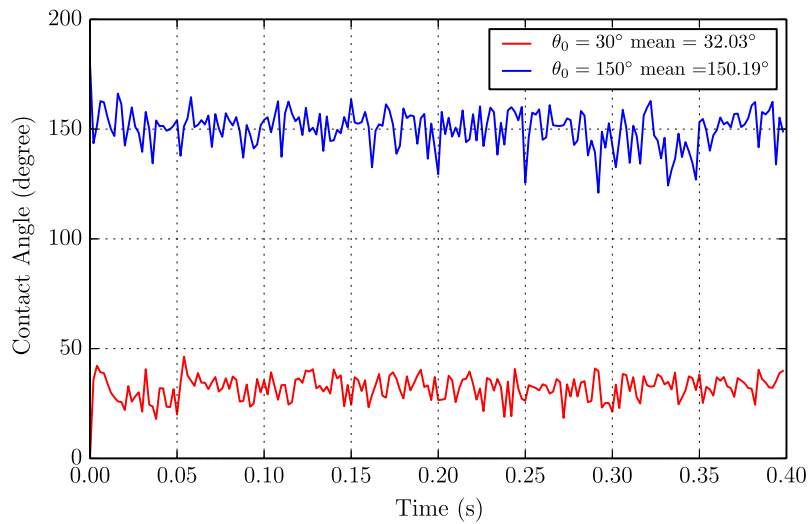

Fig. 8. Time variation of the contact angle of a 3D sessile drop for the case of wetting ($\theta = 30°$) and dewetting ($\theta = 60°$) contact angles. The droplets were initiated from the geometry of hemisphere resting on a solid surface.

3.4. Drop impact on liquid film

We simulate the splash of a droplet on a film of the same liquid using the introduced method, after validations. The famous photo of the milk crown by Edgerton and Killian (1954) has inspired a number of research works to understand the instability that leads to formation of a crown after a drop of milk impacts a thin liquid film. A thin liquid sheet, ejects immediately from the neck of the impact. Shortly after a uniform splash sheet is formed, surface ten-

sion effects begin to dominate and the phenomenon becomes non axisymmetric due to instabilities. The initial part of the splash is driven by mostly inertial effects, and this was studied by axisymmetric simulations (Josserand and Zaleski, 2003) and also by free surface SPH simulations (Nair and Tomar, 2014).

The non dimensional parameters—Weber Number ($We_{drop} = \rho v^{*2} d/\sigma$) and inertia ratio ($\alpha = d/h^{*}$, where d is the diameter of the drop and h^{*} is the thickness of the liquid film)—influence the formation of secondary droplets(Krechetnikov and Homsy,
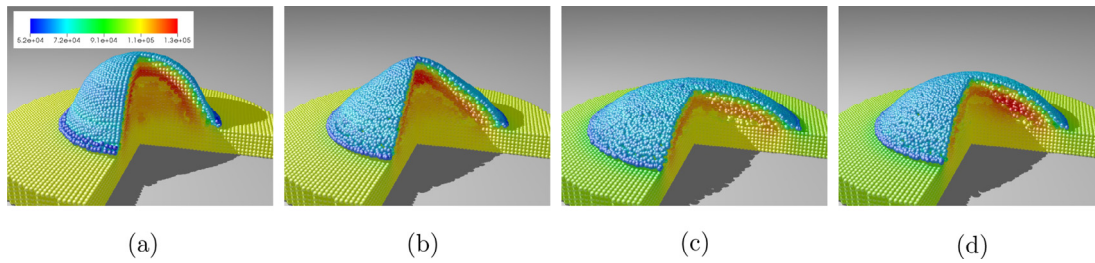
Fig. 9. Pressure field within a 3D sessile drop with contact angle 30° at different times as it relaxes to an equilibrium shape.

Table 1
The capillary rise height for different capillary tube diameters (2D).

Width (mm)	Height	
	Analytical	SPH
0.50	5.01	5.12
0.75	2.78	2.95
1.00	1.56	1.31

2009). The splashing regime encompasses a variety of different morphologies depending on the size and distribution of these droplets (Krechetnikov and Homsy, 2009). Whether this regime can be explained by a instability mechanism or multiple mechanisms remains an open question (Agbaglah and Deegan, 2014; Fullana and Zaleski, 1999) today.

We simulate a 3 mm diameter drop splashing on a liquid film impacting at a velocity of 1.8 m/s on a liquid sheet of height 0.4 mm, set as a square trough periodic in both the horizontal directions. The surface tension coefficient for the fluid is set to 0.03505 N/m, corresponding to experiments with milk drops in Krechetnikov and Homsy (2009). This corresponds to a Weber number of 273. An initial particle spacing of 0.05 mm is chosen with a smoothing length 3.0 times the initial spacing. Fig. 11 shows the simulation at different time instances, colored by velocity magnitude. In Fig. 11d, the onset of an azimuthal undulation is clearly seen. This undulation clearly compares to the splash crown fingers in experiments: 20 crests and troughs are seen in Fig. 11 in agreement with the number of sub droplets observed in experiments of milk crown splash (see Fig. 2 in Krechetnikov and Homsy (2009)) for the corresponding Weber and inertia numbers.

Lattice Boltzmann Ming and Jing (2014) and DNS (Rieber and Frohn, 1999) simulations have been performed with the imposition of a perturbation of a given wave number or a Gaussian noise,

respectively on the liquid film, to trigger the instability. In our simulations no perturbations are imposed, but the noise inherent in SPH method (see Fig. 5) triggers the crown forming instability. Splash crown simulations in Aly et al. (2013) also make use of ISPH, where particles at the free surface are identified to apply the Dirichlet boundary condition for pressure. Since such a BC would restrict pressure gradients in the direction tangential to the free surface, discernible flow features were not visible in their simulation of the splash crown. Identifying particles for application of free surface is known to deteriorate the order of accuracy and result in spraying of particles during splashes (Nair and Tomar, 2014; Asai et al., 2012). In contrast, the free surface in our simulation is smooth and the features of the splash are discernible.

Fig. 12 shows the thickening of the rim of the crown followed by folding of the rim as the expansion of the crown comes to a halt. The arrows indicate the instantaneous velocity of the surface and shows no source of circulation. The temporal evolution of the crown is shown in Fig. 13a. The red markers show the position of the rim of the splash wall over-shooting its base as the base of the splash stops expanding. Fig. 13b show the non-dimensionalized radius of base of the splash wall having a power law dependence on the non-dimensionalized time. The theoretical results by Yarin and Weiss (1995) predict the following power law relation:

$$\frac{r_b}{D} = k\hat{t}^{1/2}. \tag{29}$$

Here, r_b is the radius of the splash wall at its base, D is the diameter of the drop, k is a constant that depends on the velocity distribution inside the wall of the splash and $\hat{t} = tV/D$ is the non-dimensional time, where V is the impact velocity of the drop. The slope of line in Fig. 13b has a value 0.482 which closely corresponds to the square root dependence on time.
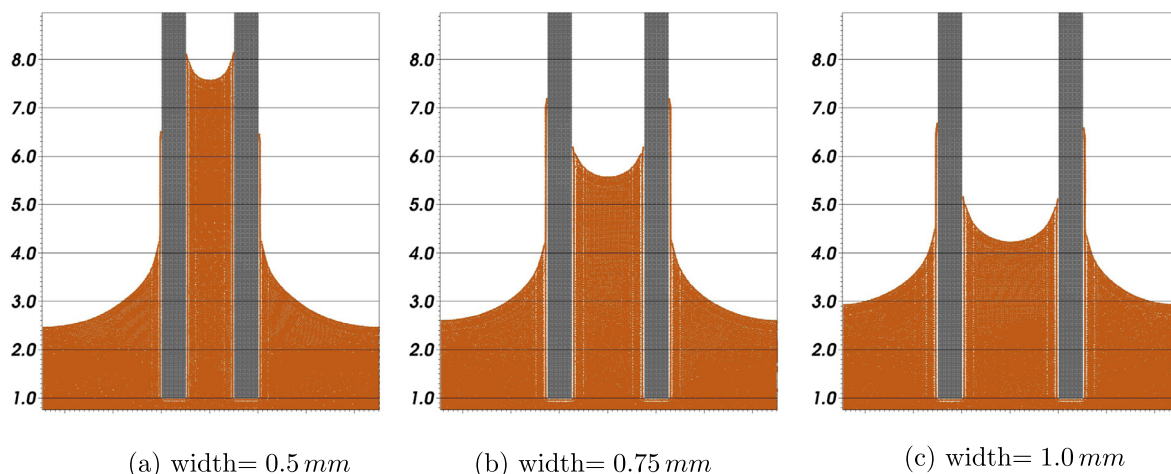

(a) width= 0.5 mm   (b) width= 0.75 mm   (c) width= 1.0 mm

Fig. 10. Capillary rise for different tube diameters.

(a) $t = 0.2\,ms$ (b) $t = 1.7\,ms$ (c) $t = 3.45\,ms$

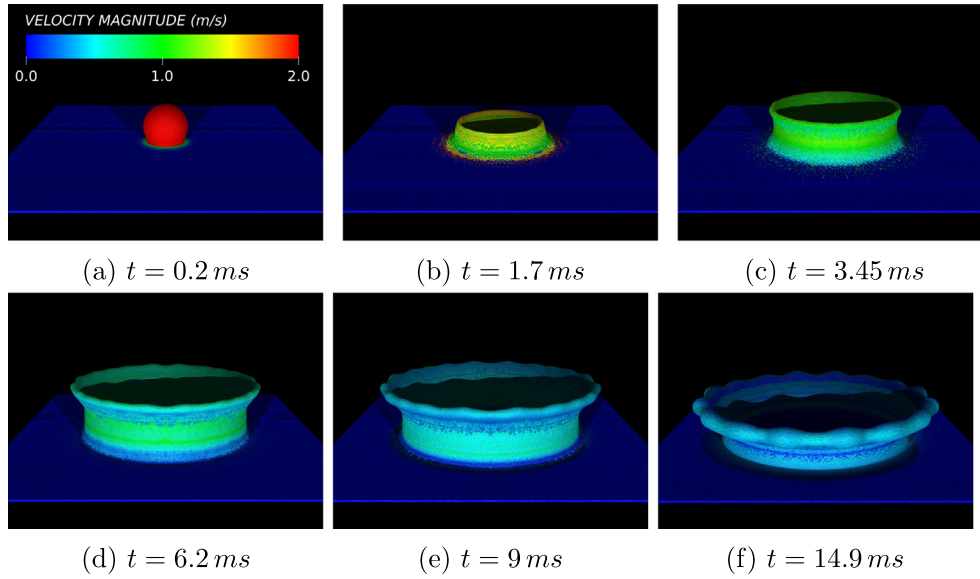(d) $t = 6.2\,ms$ (e) $t = 9\,ms$ (f) $t = 14.9\,ms$

Fig. 11. Impact of a droplet on a liquid film with a drop-Weber number, $We_{\text{drop}} = 273$ and a film-Weber number, $We_{\text{film}} = 36.5$. The fluid particles are colored by magnitude of velocity, legend on the first image, a.
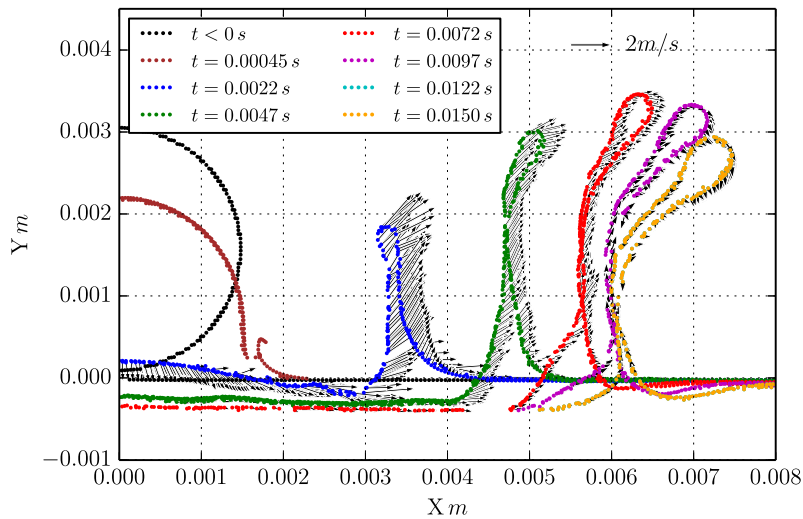

Fig. 12. Cross section profile of the splash at different time instances. The grey arrows show the velocity direction of each particle on the surface.

(a) Evolution of crown rim and base   (b) Evolution of base of crown
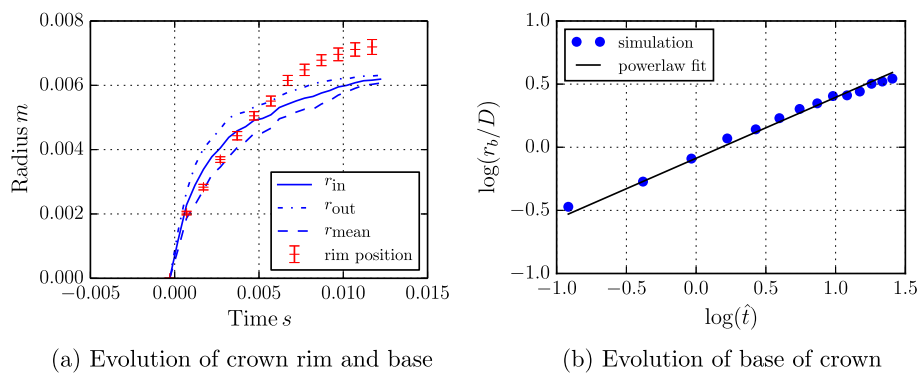
Fig. 13. Time evolution of the splash crown, measured at one vertical plane: r_{in}–inner radius of base of crown, r_{out}–outer radius of base, r_{mean}–mean radius of base of the crown. (a) The center and position of the rim at edge of the crown is shown by red markers to scale. (b) Power law dependence of non-dimensional base radius on non-dimensional time.
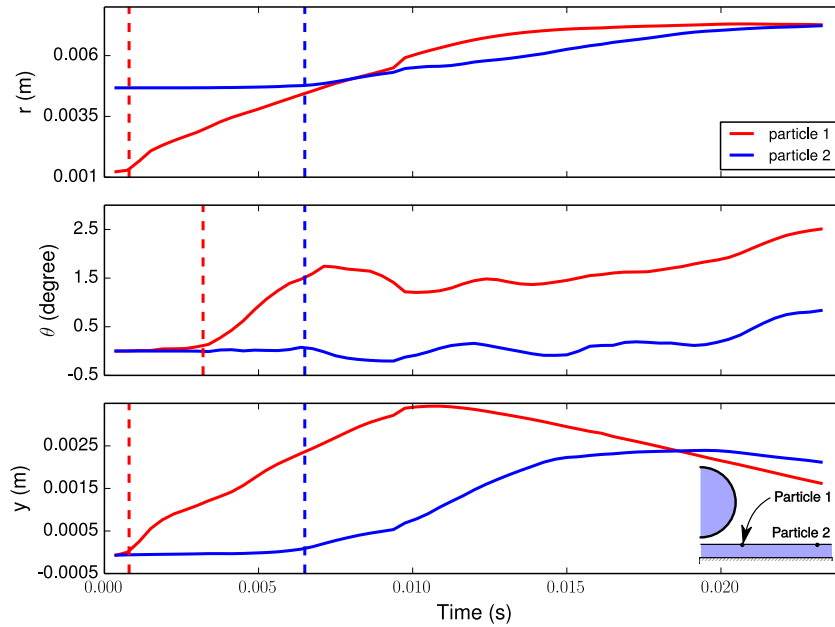
Fig. 14. Trajectory of two material points in the liquid film.

The onset of the instability in the splash can be observed as we follow two particles in different location on the initial liquid film as shown in Fig. 14. Particle 1 and 2 are chosen as shown in the inset sketch, and are followed as the splash front propagates through them. In the top part of the figure showing radial displacement, both particles are radially displaced by the splash front, as soon as the wave touches them. In the middle of Fig. 14, particle 1 is at the azimuthal location ($\theta = 0$) for a brief period of time until the instance marked by the red dashed line, after which the particle is azimuthally displaced ($\theta \neq 0$). Particle 2, however is azimuthally displaced right when the splash front reaches it. The vertical displacement also follows trend of the radial displacement. There is therefore a 'throw' of the free surface radially and vertically as a wave propagates through it. At some location between the initial positions of particle 1 and 2 the axial symmetry of the wave breaks due to instabilities in the splash crown. This observation is presented to show the advantage a Lagrangian method in tracking instabilities.

4. Dynamic liquid bridge breakage

In wet granulation processes, agglomeration of granules is a critical step for successful simulations using macroscopic simulation methods such as Discrete Element Method (DEM) (Tsunazawa et al., 2016) or Monte Carlo methods (Hussain et al., 2013). The analytical criteria used to decide whether capillary bridges will be formed during collision of wet particles for given liquid volume and approach speeds is given by quasi-static considerations. Depending on the dominance of viscous or surface tension effects in the binding liquid, a specific model is used. For example, for viscous dominant binders the following critical velocity for agglomeration is given (Ennis et al., 1991):

$$v_c = \frac{3\pi\mu R_p^2}{2M_p}\left(1 + \frac{1}{e}\right)\ln\left(\frac{y}{y_a}\right), \qquad (30)$$

where y and y_a are the thickness of the liquid layer on the grain and the surface asperity on the grain, respectively. R_p, M_p and e are the radius, mass and restitution coefficient of the grains, respectively. Other class of analytical models assume a surface tension domi-

nance to compute the force between the grains for different static configurations of the liquid bridge, for example a pendular shape (Pitois et al., 2001). In reality, the bridge deforms quite rapidly and inertial forces compete with surface tension forces deforming the interface non-linearly and a general analytical solution to the problem is difficult.

We performed a range of simulations of colliding wet spheres to find the critical velocity at which the particles stop agglomerating. This is compared to results from the purely viscous analytical model given in Eq. (30) and a numerical result using a grid based method (Kan et al., 2015). Two solid spheres of diameter 50 µm are considered, with a fluid drop of total volume 1072 µm³ divided into two drops and placed as sessile drops on both the spheres. The viscosity and surface tension of the liquid are 0.001 Nsm⁻² and 0.071 N/m respectively. These simulation parameters are similar to those used in Kan et al. (2015) for a similar study of dynamic liquid bridges. The initial particle spacing is 0.75 µm and the smoothing length is set to 3.0 times the initial particle spacing. One of the solids is launched at the other; upon contact of the liquid surfaces the drops coalesce and a liquid bridge is formed. The collision between the rigid solid spheres is assumed to be purely elastic (restitution coefficient, $e = 1$) and takes place at a point immersed within the liquid bridge.

In Fig. 15, liquid bridge configuration at different time instances for two different approach velocities are shown. The rupture of liquid bridge following collision of the solid spheres is shown in Fig. 15b for an approach velocity of 5 m/s, which is beyond the critical value for agglomeration. The liquid bridge thins to form a near cylindrical filament before rupture. The filament then breaks and relaxes to a satellite drop. In Fig. 15a, on the other hand, the liquid bridge sustains itself and causes agglomeration of the solids. In any numerical approach based on continuum description the exact instance of rupture of a material is a resolution dependent phenomena. In the presented method the liquid bridge ought to thin down until the bridge is as wide as the discretization length. However rupture results from a balance of inertia, viscous, pressure gradient and surface tension forces. In Fig. 16 the pressure field in the cross section of the liquid bridge just before rupture is shown. As the inertial force due to the separating particles tends to rupture the bridge, the increased pressure within the ends of
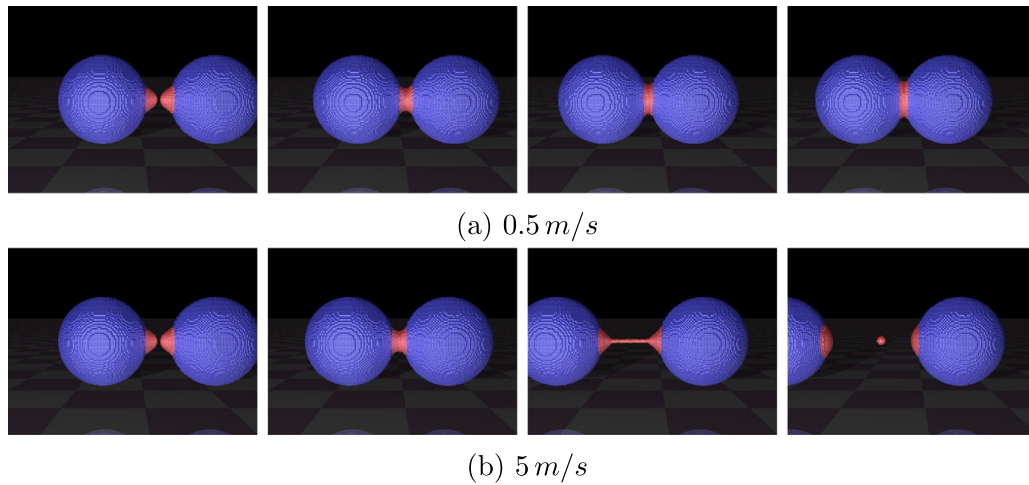
(a) $0.5\,m/s$

(b) $5\,m/s$

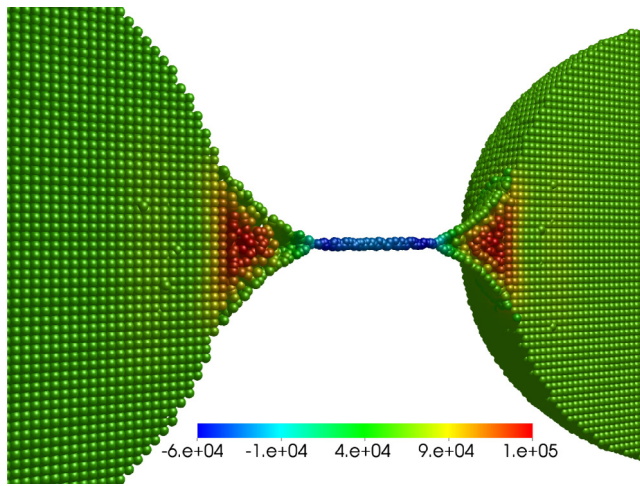**Fig. 15.** Time instances of collision of two wet solid spheres, for different approach velocities.

Fig. 16. Pressure field at the cross section of the liquid bridge just before rupture, for the case of approach velocity of 5 m/s.

In Fig. 17 the distance between the two solid spheres and relative velocity are shown as a function of times. For the smaller velocity considered (Fig. 17a), the bridge sustains and results in the particles bouncing off of each other repeatedly while remaining agglomerated. For velocity larger than critical value (Fig. 17b), the bridge ruptures and particles depart at constant velocities following rupture. A series of simulations were performed and a value of 1.1 m/s is found to be the critical velocity for agglomeration of the solid spheres. This value is about an order of magnitude higher than that predicted by the analytical model given by Eq. (30): a value of 0.16 m/s. In a similar study using a constrained interpolation method with a VOF model for interface predicted a critical velocity of 2.6 m/s (Kan et al., 2015). The reason for this discrepancy should depend on the resolution of the interface near the rupture and requires verification with experiments yet to be published. However a clear underprediction of critical velocity by a widely used analytical model is evident. With a series of numerical experiments very accurate models for the micromechanics of collision/agglomeration can therefore be developed for different regimes of viscous and surface tension forces, using the introduced ISPH method.

5. Conclusion

Incompressible Smoothed Particle Hydrodynamics (ISPH), a more accurate and robust variant of the SPH method is improved

the bridge compared to the pressure at the middle of the bridge results in a pressure gradient force that tries to oppose the inertial force of separation. The pressure field is smooth even when the liquid bridge thins down to the width of the discretization length, showing the robustness of the approach.
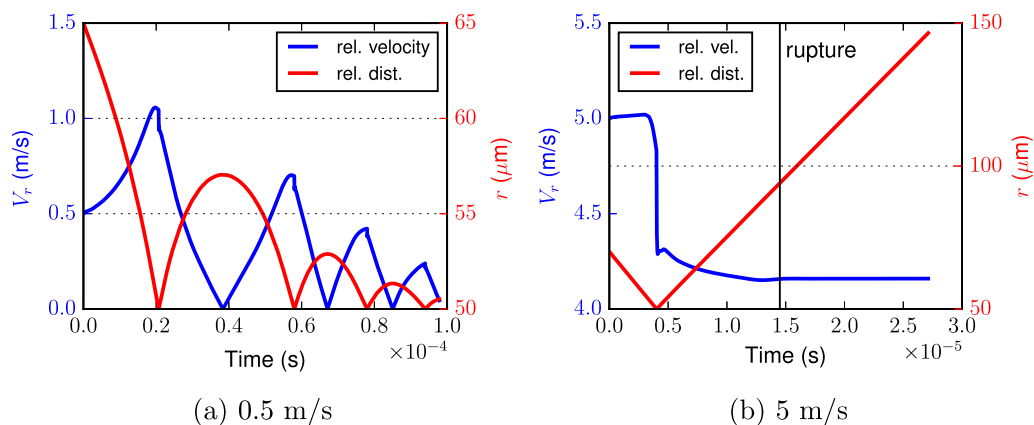

(a) 0.5 m/s

(b) 5 m/s

Fig. 17. Relative velocity (left y-axis) and distance (right y-axis) between colliding wet solid spheres for different approach speeds.

in scope to include freesurface surface tension and wetting problems based on a pairwise force model. This method superimposes a molecular dynamics fluid over a continuum incompressible fluid. Remarkably, this improved meshless method is competent for studying realistic complex flows encountered in engineering applications as demonstrated through three dimensional simulations of dynamic capillary phenomena. However, coupling a discrete system to a continuum system opens up challenges in the right choice of discretization parameters. The kinetic energy of fluctuations play an import role in accuracy of the method and this needs further attention.

Acknowledgements

Appendix A. Supplementary material

Supplementary data associated with this article can be found, in the online version, at https://doi.org/10.1016/j.ces.2017.10.042.

References

Adami, S., Hu, X., Adams, N., 2010. A new surface-tension formulation for multiphase sph using a reproducing divergence approximation. J. Comput. Phys. 229 (13), 5011–5021.
Agbaglah, G., Deegan, R., 2014. Growth and instability of the liquid rim in the crown splash regime. J. Fluid Mech. 752, 485–496.
Akinci, N., Akinci, G., Teschner, M., 2013. Versatile surface tension and adhesion for sph fluids. ACM Trans. Graph. 32 (6), 182.
Allen, M.P., Tildesley, D.J., 1989. Computer Simulation of Liquids. Oxford University Press.
Aly, A.M., Asai, M., Sonda, Y., 2013. Modelling of surface tension force for free surface flows in isph method. Int. J. Numer. Meth. Heat Fluid Flow 23 (3), 479–498.
Asai, M., Aly, A.M., Sonoda, Y., Sakai, Y., 2012. A stabilized incompressible sph method by relaxing the density invariance condition. J. Appl. Math., 139583
Bøckmann, A., Shipilova, O., Skeie, G., 2012. Incompressible {SPH} for free surface flows. Comput. Fluids 67 (0), 138–151.
Brackbill, J., Kothe, D.B., Zemach, C., 1992. A continuum method for modeling surface tension. J. Comput. Phys. 100 (2), 335–354.
Colagrossi, A., Landrini, M., 2003. Numerical simulation of interfacial flows by smoothed particle hydrodynamics. J. Comput. Phys. 191 (2), 448–475.
Colagrossi, A., Souto-Iglesias, A., Antuono, M., Marrone, S., 2013. Smoothed-particle-hydrodynamics modeling of dissipation mechanisms in gravity waves. Phys. Rev. E 87 (2), 023302.
Dehnen, W., Aly, H., 2012. Improving convergence in smoothed particle hydrodynamics simulations without pairing instability. Mon. Not. R. Astron. Soc. 425 (2), 1068–1082.
DussanV, E., 1976. Moving contact line-slip boundary-condition. J. Fluid Mech. 77 (OCT 22), 665–684.
Edgerton, H.E., Killian, J.R., 1954. Flash!: Seeing the Unseen by Ultra High-Speed Photography. CT Branford Co.
Ennis, B.J., Tardos, G., Pfeffer, R., 1991. A microlevel-based characterization of granulation phenomena. Powder Technol. 65 (1–3), 257–272.
Fullana, J.M., Zaleski, S., 1999. Stability of a growing end rim in a liquid sheet of uniform thickness. Phys. Fluids 1994-present 11 (5), 952–954.
Hirschler, M., Oger, G., Nieken, U., Le Touzé, D., 2017. Modeling of droplet collisions using smoothed particle hydrodynamics. Int. J. Multiphase Flow 95, 175–187.
Hirt, C.W., Nichols, B.D., 1981. Volume of fluid (vof) method for the dynamics of free boundaries. J. Comput. Phys. 39 (1), 201–225.
Hussain, M., Kumar, J., Peglow, M., Tsotsas, E., 2013. Modeling spray fluidized bed aggregation kinetics on the basis of monte-carlo simulation results. Chem. Eng. Sci. 101, 35–45.

Josserand, C., Zaleski, S., 2003. Droplet splashing on a thin liquid film. Phys. Fluids 15 (6), 1650–1657.
Kan, H., Nakamura, H., Watano, S., 2015. Numerical simulation of particle–particle adhesion by dynamic liquid bridge. Chem. Eng. Sci. 138, 607–615.
Krechetnikov, R., Homsy, G.M., 2009. Crown-forming instability phenomena in the drop splash problem. J. Colloid Interface Sci. 331 (2), 555–559.
Lee, E.-S., Moulinec, C., Xu, R., Violeau, D., Laurence, D., Stansby, P., 2008. Comparisons of weakly compressible and truly incompressible algorithms for the sph mesh free particle method. J. Comput. Phys. 227 (18), 8417–8436.
Liu, M., Liu, G., 2010. Smoothed particle hydrodynamics (sph): an overview and recent developments. Arch. Comput. Meth. Eng. 17 (1), 25–76.
Mikami, T., Kamiya, H., Horio, M., 1998. Numerical simulation of cohesive powder behavior in a fluidized bed. Chem. Eng. Sci. 53 (10), 1927–1940.
Ming, C., Jing, L., 2014. Lattice boltzmann simulation of a drop impact on a moving wall with a liquid film. Comput. Math. Appl. 67 (2), 307–317.
Monaghan, J., 1989. On the problem of penetration in particle methods. J. Comput. Phys. 82 (1), 1–15.
Monaghan, J.J., 1994. Simulating free surface flows with sph. J. Comput. Phys. 110 (2), 399–406.
Morris, J.P., 2000. Simulating surface tension with smoothed particle hydrodynamics. Int. J. Numer. Meth. Fluids 33 (3), 333–353.
Morris, J.P., Fox, P.J., Zhu, Y., 1997. Modeling low reynolds number incompressible flows using sph. J. Comput. Phys. 136 (1), 214–226.
Nair, P., Tomar, G., 2014. An improved free surface modeling for incompressible sph. Comput. Fluids 102, 304–314.
Nair, P., Tomar, G., 2017. A study of energy transfer during water entry of solids using incompressible sph simulations. Sādhanā 42 (4), 517–531.
Nugent, S., Posch, H., 2000. Liquid drops and surface tension with smoothed particle applied mechanics. Phys. Rev. E 62 (4), 4968.
Peskin, C.S., 2002. The immersed boundary method. Acta Numer. 11, 479–517.
Pitois, O., Moucheront, P., Chateau, X., 2001. Rupture energy of a pendular liquid bridge. Eur. Phys. J. B 23 (1), 79–86.
Popinet, S., 2009. An accurate adaptive solver for surface-tension-driven interfacial flows. J. Comput. Phys. 228 (16), 5838–5866.
Rayleigh, L., 1879. On the capillary phenomena of jets. Proc. R. Soc. Lond. 129 (196–199), 71–97.
Renardy, M., Renardy, Y., Li, J., 2001. Numerical simulation of moving contact line problems using a volume-of-fluid method. J. Comput. Phys. 171 (1), 243–263.
Rieber, M., Frohn, A., 1999. A numerical study on the mechanism of splashing. Int. J. Numer. Meth. Heat Fluid Flow 20 (5), 455–461.
Rowlinson, J.S., Widom, B., 2013. Molecular Theory of Capillarity. Courier Corporation.
Säckel, W., Nieken, U., 2016. Structure Formation within Spray-Dried Droplets; Mathematical Modelling of Spray Polymerisation. Springer International Publishing, Cham, pp. 89–125.
Szewc, K., Pozorski, J., Minier, J.-P., 2012. Analysis of the incompressibility constraint in the smoothed particle hydrodynamics method. Int. J. Numer. Meth. Eng. 92 (4), 343–369.
Tartakovsky, A., Meakin, P., 2005. Modeling of surface tension and contact angles with smoothed particle hydrodynamics. Phys. Rev. E 72 (2), 026301.
Tartakovsky, A.M., Meakin, P., 2006. Pore scale modeling of immiscible and miscible fluid flows using smoothed particle hydrodynamics. Adv. Water Resour. 29 (10), 1464–1478.
Tartakovsky, A.M., Panchenko, A., 2016. Pairwise force smoothed particle hydrodynamics model for multiphase flow: surface tension and contact line dynamics. J. Comput. Phys. 305, 1119–1146.
Tomar, G., Biswas, G., Sharma, A., Agrawal, A., 2005. Numerical simulation of bubble growth in film boiling using a coupled level-set and volume-of-fluid method. Phys. Fluids 17 (11), 112103.
Tsunazawa, Y., Fujihashi, D., Fukui, S., Sakai, M., Tokoro, C., 2016. Contact force model including the liquid-bridge force for wet-particle simulation using the discrete element method. Adv. Powder Technol. 27 (2), 652–660.
Violeau, D., 2012. Fluid Mechanics and the SPH Method: Theory and Applications. Oxford University Press.
Violeau, D., Rogers, B.D., 2016. Smoothed particle hydrodynamics (sph) for free-surface flows: past, present and future. J. Hydraul. Res. 54 (1), 1–26.
Wendland, H., 1995. Piecewise polynomial, positive definite and compactly supported radial functions of minimal degree. Adv. Comput. Math 4 (1), 389–396.
Yabe, T., Xiao, F., Utsumi, T., 2001. The constrained interpolation profile method for multiphase analysis. J. Comput. Phys. 169 (2), 556–593.
Yarin, A., Weiss, D., 1995. Impact of drops on solid surfaces: self-similar capillary waves, and splashing as a new type of kinematic discontinuity. J. Fluid Mech. 283, 141–173.
Ye, Q., Domnick, J., Scheibe, A., Pulli, K., 2005. Numerical simulation of electrostatic spray-painting processes in the automotive industry. In: High Performance Computing in Science and Engineering'04. Springer, pp. 261–275.
Zhang, M., 2010. Simulation of surface tension in 2d and 3d with smoothed particle hydrodynamics method. J. Comput. Phys. 229 (19), 7238–7259.